Ultra-rapid laser protein micropatterning: screening for directed polarization of single neurons

NIH-PA Author Manuscript

NIH-PA Author Manuscript

NIH-PA Author Manuscript

Ultra-Rapid Laser Protein Micropatterning: Screening For Directed Polarization of Single Neurons

Mark A. Scott[1,2], **Zachary D. Wissner-Gross**[1,3], and **Mehmet Fatih Yanik**[2,4,*]

[1]Harvard-MIT Division of Health, Science, and Technology, 77 Massachusetts Avenue, Cambridge, MA 02139, USA

[2]Department of Electrical Engineering and Computer Science, Massachusetts Institute of Technology, 77 Massachusetts Avenue, Cambridge, MA 02139, USA

[3]Department of Physics, Harvard University, 17 Oxford Street, Cambridge, MA 02138, USA

[4]Department of Biological Engineering, Massachusetts Institute of Technology, 77 Massachusetts Avenue, Cambridge, MA 02139, USA

Abstract

Protein micropatterning is a powerful tool for studying the effects of extracellular signals on cell development and regeneration. Laser micropatterning of proteins is the most flexible method for patterning many different geometries, protein densities, and concentration gradients. Despite these advantages, laser micropatterning remains prohibitively slow for most applications. Here, we take advantage of the rapid multi-photon induced photobleaching of fluorophores to generate sub-micron resolution patterns of full-length proteins on polymer monolayers, with sub-microsecond exposure times, i.e. one to five orders of magnitude faster than all previous laser micropatterning methods. We screened a range of different PEG monolayer coupling chemistries, chain-lengths and functional caps, and found that long-chain acrylated PEG monolayers are effective at resisting non-specific protein adhesion, while permitting efficient cross-linking of biotin-4-fluorescein to the PEG monolayers upon exposure to femtosecond laser pulses. We find evidence that the dominant photopatterning chemistry switches from a two-photon process to three- and four-photon absorption processes as the laser intensity increases, generating increasingly volatile excited triplet-state fluorophores, leading to faster patterning. Using this technology, we were able to generate over a hundred thousand protein patterns with varying geometries and protein densities to direct the polarization of hippocampal neurons with single-cell precision. We found that certain arrays of patterned triangles as small as neurite growth cones can direct polarization by impeding the elongation of reverse-projecting neurites, while permitting elongation of forward-projecting neurites. The ability to rapidly generate and screen such protein micropatterns can enable discovery of conditions necessary to create *in vitro* neural networks with single-neuron precision for basic discovery, drug screening, as well as for tissue scaffolding in therapeutics.

Keywords

---

[*]Corresponding Author Department of Electrical Engineering and Computer Science, Massachusetts Institute of Technology, 77 Massachusetts Avenue, Room 36-834, Cambridge, MA 02139. Tel.: 617-253-1583; Fax: 617-258-5846; yanik@mit.edu.

Introduction

Protein micropatterning is a powerful technique that enables systematic analyses of cellular responses to extracellular environments[1–3], as well as the production of tissue scaffolds for directing cellular development and regeneration[4–8]. Micropatterning has been widely applied to neuroscience, including studies of axon guidance[9–11], neuron polarization[12,13], axon branching[14,15], neuromuscular junction formation[16], and the formation of *in vitro* neuronal networks[17,18,7].

Micropatterning assays can elucidate how substrate geometries, protein concentrations and gradients affect neurodevelopmental phenotypes. To explore this expansive parameter space, protein patterning methods must be both rapid and versatile to generate sufficient numbers and varieties of experimental conditions. Laser micropatterning is the most versatile method for producing high-resolution multi-protein patterns with complex geometries and gradients. It enables the user to define any pattern via software, enabling rapid experimentation without the need to produce new photomasks or other hardware for each pattern design. Laser micropatterning also allows easy and precise alignment of multiple proteins by sequential patterning steps[19–21], without the need for aligning multiple stamps as in micro-contact printing, a process which is error-prone[22]. Despite these advantages, laser micropatterning remains prohibitively slow for many applications. Unlike microcontact printing[23], or illumination using a mask[24], where processing time is independent of patterning area, scanning time in laser micropatterning increases linearly with the surface area to be patterned. There exist a variety of laser micropatterning techniques in the literature, including monolayer ablation[19,25], uncaging of binding sites[20], photoinitiator-induced cross-linking[21], protein inactivation[26], and fluorophore photobleaching[27–29]. To date, none of these laser scanning approaches have achieved a patterning speed suitable for performing large-scale assays with tens of thousands of protein patterns.

Photobleaching of fluorophores, such as biotin-4-fluorescein (B4F), to create reactive species has been shown to be an effective method for laser micropatterning of biotinylated proteins[29,28]. Other studies have shown that fluorescein photobleaching occurs faster in two-photon than in one-photon fluorescence microscopy[30–32]. One-photon photobleaching of fluorescein occurs predominantly via a reaction between molecular oxygen and the triplet excited state fluorescein, resulting in the generation of a singlet oxygen that can oxidize the fluorescein radical[33]. This radical is can then crosslink with a nearby surface, enabling the patterning of fluorescein-tagged molecules[27–29]. In contrast, multi-photon photobleaching of fluorescein is thought to occur via two-photon excitation, followed by additional, stepwise absorption of photons by fluorescein in its singlet, or triplet excited states, leading to the rapid ionization of fluorescein in a fast, oxygen independent manner[31]. While detrimental for two-photon imaging studies, we hypothesized that this increased rate of photobleaching could enable rapid, multi-photon laser micropatterning of fluorescein-linked molecules onto a surface.

We previously demonstrated patterning of poly-D-lysine (PDL) using multi-photon photocoupling of fluorescein onto a short-chain, 500 Da methyl-capped polyethylene glycol (mPEG) monolayer, using a scanning speed of 200 μm/s. Here, we first demonstrate that photopatterning of biotin-4-fluorescein onto long-chain (2000 Da), acrylate-capped PEG (aPEG) monolayers enables patterning of PDL at speeds of up to 10 mm/s. Next, we show that combining this patterning approach with high-affinity, streptavidin-biotin chemistry

enables the patterning of biotinylated proteins at scan speeds of up to 1 m/s. Finally, we show that the removal of oxygen from the B4F solution results in significantly brighter patterns upon laser illumination, and enables patterning at scan speeds of 10 m/s. Taken together, our mechanically-slow galvanometer scanning-mirror setup is capable of patterning a 50×50 μm region, with ~600 nm resolution, in < 1 s, while < 10 ms patterning would be achievable with faster spinning polygonal mirror scanning setups. This represents a patterning speed of full-length proteins that is between one and five orders of magnitude faster than previous laser micropatterning methods.

The use of PEG monolayers prevents non-specific protein and cell adhesion[34], and also offers a number of other advantages. First, we show that PEG monolayers enable patterning of non-specifically adhesive biopolymers such as PDL by preventing non-specific binding on unpatterned regions. Second, the covalent attachment of the PEG monolayer to the glass enhances the stability of the protein patterns on the monolayer. Third, by using monolayers, we minimize the effects of undesired mechanical cues that are imparted to the cells, as sub-micron features as small as 14 nm have been shown to affect neurite outgrowth[35]. Otherwise, such undesired mechanical cues can override the effects of the specific chemical cues patterned on the substrate.

To demonstrate the utility and the flexibility of our laser micropatterning system, we generated more than a hundred thousand patterns, at scan speeds of 10 mm/s, with varying geometries and PDL densities to identify patterns that directed the polarization of single neurons. During polarization, the longest neurite typically becomes an axon, while the remaining neurites form shorter dendrites[36]. Polarization is regulated *in vivo* by diffusible guidance cues, morphogens, growth factors, and adhesion molecules[37]. *In vitro* protein patterns[17,38,39] and microfluidic devices[40] have been developed to direct polarization. Most successfully, millimeter-scale triangles have previously been used to construct asymmetric "diode" transmission lines, oscillators, and logic gates, but these two-dimensional patterns unidirectionally funneled hundreds of axons with little control over single-neuron polarization or connectivity[17]. To direct the polarization of individual neurons and guide individual axons, we scaled-down this geometry by two orders of magnitude to determine whether quasi-one-dimensional triangular patterns (whose widths are on the length scale of growth cones) can induce asymmetric neurite outgrowth, and lead to directed polarization of single neurons. We found that both the geometry and ligand density have significant effects on the resulting neuron morphology, that the smallest triangles supported the longest neurites, and that reducing patterned PDL density enabled longer neurite growth on larger triangles. MAP2 and dephosphorylated Tau-1 immunostaining was used to confirm that directed polarization was occurring. Using time-lapse microscopy, we showed that the neurite length asymmetry is achieved by trapping neurites growing in the "reverse" direction, since their growth cones are unable to cross from the wide base of one triangle to the narrow apex of the next triangle, while "forward" projecting growth cones are funneled between adjacent triangles. Such screens to identify protein patterns that control neuronal growth and connectivity may enable construction of *in vitro* neural networks with single-neuron precision.

Results

Formation of PEG monolayers

To produce high-contrast protein patterns, the glass substrate must be modified with a chemistry that prevents binding of proteins to regions that are not illuminated by the laser, while enabling efficient coupling of B4F upon illumination. To find a suitable chemistry, we prepared substrates uniformly coated with different PEG monolayers with varying molecular weights, coupling chemistries, and functionalized caps.

We coupled PEG to cleaned glass coverslips using either triethoxysilane or trichlorosilane cross-linking. Alternatively, to achieve PEG monolayers with variable end-groups, we first functionalized the glass with amine groups, and then we added N-Hydroxysuccinimide-PEG (NHS-PEG) to form a PEG monolayer (Fig 1a). By measuring water contact angles, we observed the predicted changes in surface hydrophobicity at each step, and demonstrated that the intermediate amine monolayer is necessary for the formation of a PEG monolayer (Fig S1a). We also showed that the relation between contact angle and NHS-PEG concentration followed a Langmuir isotherm (Fig S1b).

We found that non-specific adhesion of PDL was minimized using the methyl-capped, 500 Da, PEG (mPEG500) monolayer coupled via trichlorosilane (TCS) chemistry, while the triethoxysilane (TES) coupled mPEG2000 monolayer exhibited the most non-specific adhesion, as measured by residual background fluorescence after 10 min incubation with fluorescent PDL (Fig 1b). The NHS-amine coupled monolayers demonstrated an intermediate level of PDL adhesion, with increasing levels of adhesion as the PEG chain-length increased, and no difference was observed between monolayers formed using acrylate-capped (aPEG) and methyl-capped PEG. Since trichlorosilane-functionalized mPEG is only commercially available at low molecular weights (500 Da), for all subsequent experiments, high molecular weight PEG monolayers (2000 Da) were instead formed using the two-step, NHS-amine coupling chemistry.

Rapid laser micropatterning of full-length proteins

To perform protein patterning on the various PEG monolayers, we built a custom photopatterning setup, as shown in Fig 1c. A Ti:sapphire femtosecond laser was tuned to 780 nm, near the two-photon absorption maximum of fluorescein[41], and the beam was focused using a 40x, 0.9 NA, air objective. The laser was scanned using two-axis galvanometer scanning mirrors across the surface of PEGylated coverslips, with laser power controlled by a high-bandwidth (8 MHz) electro-optic modulator (EOM). Since the speed of the scanning mirrors could not exceed 10 mm/s in our setup, higher speeds were simulated using pulse-width modulation (PWM), achieved by mixing the EOM signal with a 100 kHz square wave with varying duty cycles (Fig S2), thereby modulating the dwell time of the laser. For example, a 10% duty cycle applied to a scan speed of 10 mm/s simulated a scan speed of 100 mm/s. A Nikon Perfect Focus system was used to maintain laser focus throughout the patterning process.

Biotin was coupled to the monolayer surface via multi-photon photobleaching, and subsequent free radical coupling of biotin-4-fluorescein (B4F) to the PEG monolayer (Fig 1d). Streptavidin was then added to the patterned B4F, and after coupling to the underlying biotin, the remaining free biotin binding sites were used to pull down biotinylated proteins. Alternatively, adhesive proteins such as PDL adsorbed directly to the underlying B4F without the need for streptavidin.

We measured the brightness of patterns of fluorescent streptavidin on B4F patterned mPEG500, mPEG5000, aPEG5000, and aPEG3500 monolayers, using scan speeds of 10 mm/s and a scan line separation of 0.25 μm (Fig 2a). Patterning on longer chain PEG monolayers (MW 2000 Da) resulted in a ~20-fold increase in pattern brightness compared with mPEG500, and using acrylated functionalized caps provided an additional ~2-fold increase in pattern brightness when compared with methyl-capped monolayers.

Next, we produced arrays of square patterns of fluorescently-labeled PDL and streptavidin at different laser powers and scanning speeds on surfaces of mPEG500 (which we used previously[27]), BSA (used by Costantino et al.[29,28]) and an aPEG3500 monolayer. While PDL pattern brightness increased monotonically with laser power and dwell time (the

inverse of scan speed), streptavidin patterns exhibited an overexposure behavior for high dwell times and laser powers (Fig 2b). PDL patterns could be formed at higher scan speeds on an aPEG3500 monolayer than on mPEG500 (Fig 2c,i), with higher powers necessary to achieve patterns at higher scan speeds (Fig 2c,ii). We found that PDL patterns did not form on BSA, since BSA did not block adhesion of PDL to the underlying glass (see Fig 1b), resulting in a significant background that was as bright as the patterned area (data not shown). Streptavidin patterns were also consistently brighter at all scan speeds on an aPEG3500 monolayer when compared with either BSA or mPEG500 (Fig 2c,iii). Furthermore, using high laser powers, streptavidin could be patterned at scan speeds of up to 1 m/s (Fig 2c,iv). As expected for a multi-photon process, we found that pattern brightness depended strongly on the height of the laser focal plane above the glass, with the brightest patterns being achieved when the laser was focused at the interface of the glass and B4F solution (Fig S3).

We further analyze the kinetics of the photopatterning of B4F by studying how streptavidin brightness varies over a range of laser powers and scan speeds (Fig 2c,iv). Others have found that the multi-photon bleaching rate of fluorescein is well modeled by the power law:

$$\Gamma = A P^B \qquad (1)$$

Where Γ (s^{-1}) is the bleaching rate, and A and B are fitting parameters[32]. The high, ~ 0.1 pM, affinity of biotin-streptavidin interactions enables us to assume that, at low levels of laser exposure (below levels that result in surface or fluorophore saturation), every patterned molecule of B4F will be bound by a streptavidin molecule. Hence, the streptavidin pattern brightness is proportional to the surface density of patterned B4F, which itself is proportional to the product of the bleaching rate and dwell time:

$$S = \alpha \tau P^B \qquad (2)$$

Where τ is the dwell time (the reciprocal of scan speed), S is the normalized streptavidin pattern brightness, and α and B are fitting parameters. As predicted by this equation, log-log plots of streptavidin pattern brightness with laser power yielded straight lines over small power intervals (Fig 2c, iv). Over a wider range of powers, we observed increasing slopes with increasing laser power and scan speed (Table 1).

Next, we found that the pattern brightness increased asymptotically with increasing concentrations of B4F (Fig 2d). To support our hypothesis that the coupling of B4F to the PEG monolayer is governed by a radical process, we studied the effect of adding L-ascorbic acid, a radical scavenger, to the B4F solution. We found that the L-ascorbic acid shifted the streptavidin pattern brightness curve to the right, demonstrating that a radical scavenger inhibits B4F patterning in a concentration dependent manner (Fig 2e). Next, to study the effect of oxygen on patterning, we compared patterns obtained from deoxygenated and oxygenated solutions of B4F. Surprisingly, we found that purging oxygen from the B4F solution resulted in a significant leftward shift in the curve, representing an increase in patterning efficiency (Fig 2f). To test whether deoxygenation of B4F could further increase the maximum patterning speed, we demonstrated bright streptavidin patterns created with an exposure time of 100 ns (8 pulses), representing a scan speed of 10 m/s (Fig S4). To test the influence of the triplet-excited state of fluorescein on photobleaching, we added the triplet-state quencher mercaptoethylamine (MEA or cysteamine) to the B4F solution. We found that the presence of MEA significantly inhibited patterning, causing a significant rightward shift of the brightness curve (Fig S5).

To verify that biotinylated, full-length proteins can be patterned at high speeds using streptavidin as an intermediate, we showed that fluorescent patterns of biotinylated laminin

could be created at scan speeds of up to 1 m/s (Fig 2g). To assess the pattern resolution, we formed 2 µm spaced lines of streptavidin at a scan speed of 1 m/s. The resulting patterns had a full-width half-maximum (FWHM) resolution of ~ 600 nm (Fig 2h). Finally we showed that smooth, arbitrary gradients of proteins can be produced using a scan speed of 10 mm/s. The fluorescent streptavidin picture of the MIT dome, shown in Fig 2i, was produced in < 1.4 s. To summarize the various technological aspects presented thus far, laser photobleaching patterning techniques, and their corresponding laser scan speeds are shown in Table 2.

The total time required to create a protein pattern can be broken down into three parts: laser scanning time, stage motion time, and signal processing time. The laser scanning time is proportional to the scan speed, and the area to be patterned. The stage motion time is the time taken for the stepper motor stage to translate from a recently patterned region, to a new region. The signal processing time is the combined time required for translating the vectorized, geometric pattern data into voltage streams and to upload these into the buffer of the NIDaq card for output. The relative contributions to total patterning time from stage moving and signal processing times increased with laser scan speed (Fig S6). At a scan speed of 100 µm/s, the laser scanning time was rate limiting, while at the highest scan speed of 1 m/s, the signal processing and stage motion times became rate limiting.

Growth-cone-scale triangles direct polarization of individual neurons

Using our flexible and scalable rapid laser micropatterning system, we screened a variety of protein surface patterns to search for specific geometries that could direct the polarization of single hippocampal neurons. Using a scan speed of 10 mm/s, the limiting speed of our mechanically-slow scanning mirrors, we first generated 15,000 adhesive, unbiotinylated PDL triangles arrayed in columns over a 15 mm × 2.4 mm area (Fig 3a). PDL was chosen for its ability to support robust neurite outgrowth *in vitro*. Although PDL patterns produced at this scan speed are only ~ 15% of the maximal PDL brightness (see Fig 2c,iii), they were still capable of supporting neurite outgrowth. The triangles varied in size (from 60×60 µm down to 10×10 µm, width × height) and aspect ratio (from 70 µm in width down to 10 µm in width with a constant height of 30 µm) (Fig 3b). For all triangles, the width of the apex was set to 1 µm, consistent with the resolution of our laser micropatterning method. The total patterning time, defined as the sum of the laser scanning time (59 min), the stage motion time (4 min) and the signal processing time (28 min) was approximately 1.5 h.

Embryonic day 18 (E18) rat hippocampal neurons were seeded onto the patterned array. After 48 h in culture, the cells were fixed and stained for βIII-tubulin to visualize neuronal outgrowth. We defined a neuron as being topographically polarized in the forward or reverse direction relative to the underlying pattern depending on whether its longest neurite projected from base to apex or from apex to base, respectively (Fig 3b). We observed that all geometries led to a statistically significant excess of neurons polarized in the forward direction (Fig 3c) ($p < 0.05$). We found that even triangles that were 10 µm in width and height, a size similar to that of neurite growth cones, resulted in significant neurite length asymmetry ($p < 0.01$). However, triangles that were 50 µm or 70 µm wide failed to produce significantly different mean neurite lengths projecting in the forward or reverse directions (Fig 3d). When the triangle's height was fixed at 30 µm, we found that narrower (10 µm wide) triangles resulted in significantly longer *total* neurite outgrowth, defined as the sum of the forward and reverse projecting neurites, than triangles that were either 30, 50, or 70 µm in width ($p < 0.001$). These data suggest that long neurite outgrowth and efficient neurite asymmetry can be achieved using triangles with longitudinal and parallel dimensions comparable to that of growth cones.

Patterns with lower PDL density induce longer neurite outgrowth

We explored whether the patterned PDL density affected neurite outgrowth. We generated an array of 50×50 μm (width × height) triangles with different PDL surface densities by varying the laser power (Fig 4). As before, E18 hippocampal neurons were plated, fixed, and stained for βIII-tubulin after 48 h in culture.

We found that a reduction in the patterned PDL density resulted in significantly longer neurites ($p < 10^{-4}$) with mean total neurite length (the sum of mean forward and reverse lengths) increasing from ~60 μm to ~115 μm as PDL pattern concentration was reduced by 10-fold. We were unable to further decrease pattern brightness, as the patterned density of PDL approached that of the non-specific PDL adhesion to the substrate, causing neurons to cease following patterns.

MAP2 and Tau-1 immunostaining confirms directed neuron polarization

Thus far, we have demonstrated that PDL triangles can induce length asymmetry in forward and reverse projecting neurites. To check whether this topographical asymmetry reflects an underlying asymmetry in axonal and dendritic specialization, we cultured neurons on 10×10 μm and 20×20 μm triangles, and stained for Tau-1 and MAP2 after 48 h in culture (Fig 5a). We found that neurons cultured on both 10×10 μm and 20×20 μm triangles exhibited significant axonal and dendritic specialization, with 72% of the axons of polarized neurons extending in the forward direction (Fig 5b). Polarization was confirmed by the localization of dephosphorylated Tau-1 preferentially at the distal axon, and the localization of MAP2 in the dendrites, soma, and proximal axon (Fig 5c).

Time-lapse analysis: Pattern geometry inhibits elongation of "reverse" projecting neurites

To gain further insight into how neurons growing on micropatterned triangles are preferentially polarized in the forward direction, we performed time-lapse imaging over 48 hours with a temporal resolution of approximately 15 minutes. We measured the growth of neurites over time from 12 representative neurons on 20×20 μm triangles (Fig 6, Fig S7). Fig 6a shows the time course of neurites extending from a neuron which was initially exhibiting growth in the reverse direction. The neuron repeatedly attempted to extend a reverse-projecting neurite (arrow), but if the growth cone turned off the centerline of the procession of triangles, the neurite failed to find the connection to the next triangle (Fig 6b,i) and subsequently retracted (Fig 6b,ii). At the same time, the forward projecting neurite responded with a period of rapid, unhindered elongation (Fig 6b,ii-iv). Histograms, averaged over time and over all neurons, showed how often the neurite tips were found at different locations on the patterned triangles (Fig 6c). The histogram for the reverse projecting neurites displays a peak at the boundary between two triangles, demonstrating that the growth cone stalls at the triangles' boundaries when projecting in the reverse direction. Conversely, the histogram for the forward projecting neurite exhibits a flatter profile, demonstrating that the growth cone passes unimpeded in the forward direction. This directional dependence of growth cone stalling at boundaries explains the observed biased polarizing effect of these triangle ratchet patterns.

Discussion

Laser protein patterning, while enabling the mask-free production of arbitrary gradients, remained a relatively slow process for most applications. In this paper, we have demonstrated an unprecedentedly rapid laser micropatterning method for creating patterns of streptavidin and full-length, biotinylated proteins by multi-photon photobleaching of biotin-4-fluorescein (B4F). We found that using 3,500 Da, acrylated PEG (aPEG3500) monolayers as a patterning substrate provides a good balance between resisting non-specific

protein adhesion (Fig 1b) and enabling patterns of PDL at scan speeds of up to 10 mm/s, and streptavidin at speeds of up to 1 m/s (Fig 2a and Fig 2c). By varying laser power, we can create smooth gradients of proteins (Fig 2i) with submicron resolution (Fig 2h).

Optical patterning with B4F is advantageous because full-length proteins are never exposed to potentially damaging laser powers, and because B4F is relatively inexpensive, higher bath concentrations of B4F can be used to enable faster laser micropatterning. Unlike laser patterning on BSA[29,28], our use of a PEG monolayer enables patterning of highly adhesive proteins, such as PDL. Because we covalently bind the monolayer to the glass substrate, the patterns of streptavidin and biotinylated proteins are not stripped off, even after vigorous washing during solution exchange.

The high-affinity of streptavidin for the patterned biotin molecules also enabled us to study the mechanism of fluorescein photobleaching (Fig 7). We found that the sub-saturation streptavidin pattern brightness followed a power law with laser intensity (Fig 2c,iv and Eq 2), as predicted by previous studies in multi-photon photobleaching of fluoroescein[32,30]. There are many parallel chemical pathways for multi-photon photobleaching of fluorophores[42], and the slope of the power law represents the number of step-wise photon absorption events occurring in the dominant photobleaching pathway(s) at a given laser intensity.

We discovered that the exponent of this power law, extracted from the slope of the log-log plots, increased from B=2.5 (indicating involvement of both 2- and 3- photon processes) at low intensities, to B=3.2 at intermediate intensities, and to B>4 at the highest intensities. The slope we measured at low-intensities (B=2.5) closely matches that of a fluorescein photobleaching experiment performed by Chirico et al. (B=2.45) using a similar low-intensity range and wavelength (λ=770 nm)[32]. At mid-range intensities, our data (B=3.2) agrees with that presented by Patterson et al. (B=3.1), although they photobleach using light at a different wavelength (λ=710 nm). Neither of these prior studies reported a variation of the slope with power, perhaps because both experiments were carried out over a narrow range of powers (around half an order of magnitude), whereas by varying scan speeds (i.e. dwell time) to avoid saturation of surface binding sites, we were able to study the laser intensity dependence of photopatterning over two orders of magnitude. In a paper looking at multi-photon photobleaching of a pyrilium salt in a three-dimensional polymeric material, Polyzos et al. suggested that the slope increased at the highest laser powers, although no data was shown[43]. Fluorophores at higher excitation states are less stable, likely leading to faster patterning kinetics.

To compare our rate of photopatterning with that of photobleaching, we find the power (~16 mW) at which streptavidin pattern brightness reaches 10% of its saturation value at a scan speed of 100 μm/s (a dwell time of 40 ms/μm^2) from Fig 1c (iv). At this intensity and exposure time, we anticipate that ~4,000 (or 2.4%) of the B4F molecules in a 1μm^3 volume would photobleach (using fluorescein photobleaching kinetics from Chirico et al.[32]). A 100% saturated surface of streptavidin, assuming a 5.4 nm × 5.8 nm footprint[44], would have a density of ~30,000 molecules per μm^2 and thus a 10% saturated surface would have ~3,000 molecules per μm^2. Thus, the rate of B4F photobleaching and the resulting surface pattern densities are in reasonable agreement.

Importantly, the removal of oxygen from the B4F solution significantly increased streptavidin pattern brightness (Fig 2f). This is in stark contrast with results from streptavidin patterning by one-photon photobleaching, where removal of oxygen from the solution reduced pattern brightness by approximately 8-fold[45]. Yet, our observation is consistent with previous studies that have shown that singlet oxygen induced photobleaching

is not the dominant photobleaching pathway in multi-photon microscopy[31]. This observed increase in pattern brightness due to the removal of oxygen could be due to two mechanisms: First, dissolved molecular oxygen is known to quench triplet-excited fluorescein, resulting in the generation of singlet oxygen, and the return of fluorescein to its ground-state (Fig 7)[33]. Furthermore, others have suggested that multi-photon photobleaching of both GFP and Atto 532 occurs predominantly via step-wise absorption of additional photons by the fluorophore while in its triplet-excited state[42]. Thus, the removal of oxygen increases the half-life of triplet-excited fluorescein, and increases the probability of additional photon absorption and multi-photon photobleaching from this state. This mechanism is further supported by the observation that adding MEA, a triplet-state quencher[33], significantly inhibited streptavidin patterning (Fig S5). Future strategies for enhancing the speed of multi-photon patterning of fluorophores should focus on further stabilizing the triplet-excited state, to increase the probability of additional photon capture and photobleaching. A second mechanism that can explain why removing dissolved oxygen increases patterning efficiency is that oxygen is known to act as an inhibitor in free-radical polymerization reactions[46]. Thus, oxygen may be reacting with the B4F radicals and forming a less reactive radical, in essence competing with the binding of B4F to the aPEG3500 monolayer. The dominant mechanism could be elucidated by comparing the photobleaching rate of fluorescein in oxygenated, and deoxygenated solutions using fluorescence correlation microscopy.

Finally, to provide evidence for free-radical mediated cross-linking of B4F to the underlying aPEG3500 monolayer, we showed that streptavidin pattern brightness was reduced by the addition of the free radical scavenger, L-ascorbic acid, in a concentration dependent manner (Fig 2e).

The total time required to produce a pattern over a wide area can be broken down into three distinct times: the laser scanning time, the stage moving time, and the signal processing time. As laser scanning speed increases from 100 μm/s to 1 m/s, stage motion and signal processing times become the rate-limiting steps for patterning using our setup (Fig S6). To achieve patterning at the maximum speed allowed by the rate of the photopatterning chemistry, spinning polygonal mirrors could replace the mechanically-slow x-y galvanometer scan mirrors to increase the maximum attainable scan speed from 10 mm/s to 1 m/s. At speeds of 1 m/s, streptavidin pattern brightness depends approximately on the fourth power of intensity (Fig 2c, iv), thus small changes in laser power or laser focus will cause a large change in pattern brightness, and must be closely controlled by using an autofocus system such as Nikon Perfect Focus. Stage motion time could be effectively eliminated by scanning the laser in one axis, while the stage continuously translates along the perpendicular axis. Finally, the signal processing time can be significantly reduced by using a compiled code, by storing vectorized geometric data in an uncompressed form, or by using a dedicated field-programmable gate array (FPGA).

To demonstrate the flexibility and utility of our laser micropatterning system, we performed multiple screens with more than 100,000 patterned triangles, requiring a total patterning time (i.e., the total time spent scanning the laser, moving the stage, and processing the patterns in software) of only ~6 h at a scan speed of 10 mm/s. Our polarization geometry screens showed that patterns of 10×10 μm triangles are capable of both directing neuronal polarization (confirmed using Tau-1 and MAP2 immunostaining, Fig 5) and allowing long neurite outgrowth, while larger (30×30 μm and 60×60 μm) triangles, and wider aspect ratio (50×30 μm and 70×30 μm) triangles resulted in shorter neurite outgrowth (Fig 3d). The relationship between neurite outgrowth and pattern width agrees with results from recent stripe assay experiments using PC12 cells[47]. We also found that reducing the surface density of PDL enabled significantly longer neurite outgrowth on larger 50×50 μm

triangles (Fig 4). Time lapse imaging was used to observe the ratchet-effect of the triangles, where if reverse-projecting neurites venture off the centerline of the triangles, they are unable to find the next patterned triangle, and stall (Fig 6).

Others have used micron-scale triangular geometries to bias the migration of fibroblasts[48], and cell migration and neurite elongation share many intracellular processes[49]. These fibroblast migration "ratchets" achieved a migration bias (a migration preference in the forward direction) on the order of 60%. Here, we obtained a significantly higher polarization bias of 72% with the hippocampal neurons using patterns as small as neurite growth cones ($p < 0.05$). A comparison of our triangle ratchet geometry with previous directed polarization, or axon-redirecting methods is presented in Table 3. Methods that induce directed polarization, such as that presented in this paper, use geometries that influence the rate of elongation of immature neurites to coordinate which neurite becomes the axon. Methods that use axon-redirection selectively permit passage of axons in one particular direction after neurons are already polarized. The most commonly studied geometry for directing the polarization of single neurons is a "speed bump" pattern, achieving polarization biases as high as 76%[38]. These patterns combine solid lines, and dashed (speed bump) lines of adhesive proteins. A cell body, situated at the intersection of the two lines, extends its axon rapidly down the continuous protein line, while the other neurites, growing along the dashed protein lines, extend slower. Unlike the geometries presented here, these speed-bump patterns require that neuron cell bodies are positioned in specific somal adhesion sites on the patterns.

The ability to rapidly generate and screen protein micropatterns can enable discovery of the conditions necessary to create *in vitro* neural networks with single-neuron precision. Such networks may be used in basic discovery, drug screening, as well as tissue scaffolding in therapeutics.

Methods

Preparation of PEG monolayers

Glass coverslips (Matrical, Spokane, WA) were cleaned in a bath of Nanostrip (a stabilized piranha solution; Cyantek, Fremont, CA), at 65°C for 15 min. Coverslips were then sonicated in deionized (DI) water for 5 min, rinsed under running DI water, then dried under a stream of nitrogen gas. To add surface amine groups, coverslips were then transferred to an ethanol bath, heated to 70°C (as this has been shown to increase APTES cross-linking efficiency and stability[50]), containing 10% v/v amino-propyltri(ethoxy-silane) (APTES; Sigma-Aldrich, St. Louis, MO) for 30 min. Afterwards, the coverslip was rinsed in a room temperature ethanol bath, sonicated in DI water for 5 min, rinsed under running DI water, then dried under a stream of nitrogen gas. Methyl-capped N-hydroxysuccinimide-PEG-2000 (mPEG2000), or acrylate-capped N-hydroxysuccinimide-PEG-3500 (aPEG3500), obtained from JenKem Technology USA (Allen, TX), were added to 100 mM borate buffer (Invitrogen, Carlsbad, CA) to a concentration of 10 mg/ml, sonicated for 3 s to dissolve the NHS-PEG, then 5 ml of the solution was added to cover the surface of the coverslip. After 30 min, the NHS-PEG was rinsed off under running DI water and gently dried under a stream of nitrogen gas. The coverslip was then stored, protected from light, for < 1 week in a desiccator prior to use.

To create the mPEG trichlorosilane monolayers, nanostrip cleaned glass coverslips were added, under nitrogen, to a toluene bath containing 1% w/v 2-[methoxy(polyethyleneoxy)propyl]trichlorosilane (Gelest, Morrisville, PA) for 1 h. Still in the nitrogen atmosphere, coverslips were then rinsed in a fresh toluene bath, sonicated in DI

water for 5 min, and then rinsed under running DI water. Coverslips were then dried under a stream of nitrogen, and stored for < 1week in a desiccator prior to use.

To create the mPEG triethoxysilane monolayers, nanostrip cleaned glass coverslips were added to a 10% w/v solution of mPEG triethoxysilane (JenKem Technology USA) in ethanol, with pH adjusted to < 5.5 using glacial acetic acid. After 1 h , the coverslips were removed, rinsed in fresh ethanol, then sonicated for 5 min in DI water and rinsed under running DI water. Coverslips were dried under a stream of nitrogen, and stored for < 1 week in a desiccator prior to use.

Pattern Design and Signal Generation

Patterns were designed using a custom-built MATLAB interface which translated shapes or pictures into voltage data streams to control the x-y scanning mirrors and EOM voltage. The three data streams were uploaded into the data buffer of a National Instruments PXIe-6259 card and were output at a rate of 800 kSamples/sec from three analog output channels. To achieve varying laser duty cycles to simulate higher speed patterning, the analog output channel was first multiplied, using a variable-gain amplifier, with a square wave from a signal generator (see Fig S2).

Protein Patterning

200μg/ml of B4F (Invitrogen, Carlsbad, CA) in pH8 borate buffer, was added to a well, made by pushing polydimethylsiloxane (PDMS) onto the PEG-coated glass coverslip. A MAITAI femtosecond laser (Newport, Irvine, CA), with ~100 fs pulse duration and 80 MHz pulse repetition rate, was tuned to 780 nm and focused through a 0.9NA, 40X air objective, using a Perfect Focus system (Nikon Instruments, Melville, NY) to maintain focus across the field of patterning. Unless otherwise stated, patterns were formed at a scan speed of 10,000 μm/s, a laser power of 5 nJ/pulse (as measured at the sample), and a scan-line separation of 0.25μm, with a typical 50 μm × 50 μm (width × height) triangle requiring 500 ms of patterning time.

To study the effect of oxygenation of the B4F solution on patterning, B4F was purged of oxygen by bubbling nitrogen gas through the solution for 30 min, followed by addition of 200U/ml glucose oxidase and 10mM glucose to scavenge remaining oxygen. The solution was left for 10 min to allow for the scavenging of remaining oxygen prior to patterning. The oxygenated B4F solution was formed by bubbling oxygen gas through the solution for 30 min.

70-150 kDa PDL (Sigma-Aldrich) was fluorescently labeled by adding 65 μg of DyLight 594-NHS (Thermo Fisher Scientific) to 1 mg of PDL in 0.5 ml of borate buffer. After 1 h, the remaining unconjugated dye was separated by size exclusion chromatography. Streptavidin was purchased preconjugated with Alexa-Fluor 555 (Invitrogen). PDL and streptavidin were added to laser patterns of B4F at 10 μg/ml in PBS containing 3% BSA and incubated for 10 minutes prior to vigorous washing with 5 ml borate buffer. Laminin was biotinylated by mixing 1 mg/ml DyLight 594-conjugated laminin (made as described for PDL labeling) in borate buffer with biotin-PEG3500-NHS (Jenkem Technology, USA) at a 20:1 molar ratio. The biotinylated laminin was then purified from unreacted biotin-PEG3500-NHS by using size-exclusion chromatography.

Fluorescence images were acquired using a Coolsnap HQ2 CCD (Photometrics, Tucson, AZ). For measuring background adhesion of fluorescent PDL, 10 μg/ml PDL was incubated for 10 min on passivated surfaces, and an average pixel brightness was measured. To account for dark noise and fluorescent filter imperfections, this value was then subtracted from the mean pixel brightness measured for a negative control surface with no PDL

adhesion. For streptavidin and biotinylated laminin patterns, protein was added at $10\ \mu g/ml$ and incubated for 5 min. For measurement of pattern brightness, the mean pixel values for patterned regions of interest were subtracted from a mean pixel value of a background region of interest.

Dissection and Cell Culture

All animal work was approved by the MIT Committee of Animal Care and Division of Comparitive Medicine, and abided by institutional, state, and federal guidelines for animal welfare. Hippocampi were harvested from E18 Sprague Dawley rats (Charles River Laboratories, Wilmington, MA), and digested in ice-cold Hank's balanced salt solution (HBSS), buffered with 10mM HEPES, pH 7.3. The tissue was digested by a 30 min incubation in 2ml of HEPES buffered HBSS containing 20U/ml of papain (Worthington Biochem., Lakewood, NJ), 1mM EDTA and 1mM L-cysteine. Next, the tissue was rinsed three times with 8 ml of Neurobasal-B27 containing 2mM glutamine and 100U/ml penicillin/streptomycin (hippocampal culture medium). The cells were gently triturated in 1 ml of hippocampal culture medium, counted with a hemocytometer, and plated at a density of 30k cells/cm^2. The cells were maintained at 37°C, 5% CO_2 before imaging. For time-lapse imaging, cells were maintained in a microscope-mounted 37°C, 5% CO_2 incubator and imaged in brightfield continuously for 48 h using a custom-built MATLAB stage and camera controller. Light intensity was kept low (exposure time > 500 ms for the Coolsnap HQ2 camera) to minimize phototoxicity.

Immunocytochemistry

After 48 h in culture on PDL patterns, cells were fixed for 30 min in 4% paraformaldehyde, and then rinsed 3x in PBS containing 0.05% tween-20 (PBST). Cells were permeabilized by 10 min incubation in 0.01% triton-X in PBS, and then rinsed 3× in PBST. The cells were blocked for 30 minutes in PBST containing 3% BSA. Cells were then incubated in PBST containing 3% BSA with either mouse monoclonal βIII-tubulin antibody for neurite imaging, (R&D Systems, MAB1195, dilution 1:1000) for 1 h, or mouse monoclonal dephosphoTau-1 for axon identification (Millipore, dilution 1:250) with rabbit polyclonal MAP2 for dendrite identification (Millipore, dilution 1:400) overnight. After 3 rinses in PBST, cells were incubated with a fluorescently labeled conjugated secondary antibody for 30 min, and rinsed in PBST. Finally, cells were incubated in 1:10,000 dilution of DAPI for 1 min prior to a final rinse with PBST. Cells were imaged using a custom-built MATLAB scan and stitch software. .

Image and Data Analysis

Stitched fluorescence and bright field images were analyzed using ImageJ. Lengths of neurites were measured as a straight line, from the center of the nucleus, to the most distal tubulin in the growth cone, visualized with immunofluorescence. For the geometric screen, neurons with combined neurite length of less than $60\ \mu m$ were ignored to ensure that all counted neurons extended over more than one triangle. P-values for the proportions of neurons with the longest process oriented in the forward or the reverse directions of the triangles, and for tau-1/MAP2 localization data were calculated using a null hypothesis of a binomial distribution with p = 0.5. We performed paired, two-tailed t-tests to verify statistically significant differences in the lengths of forward and reverse projecting neurites, and to verify significant differences between the total neurite lengths for the geometric and PDL density screens. All error bars display standard error of the mean.

Supplementary Material

Refer to Web version on PubMed Central for supplementary material.

Acknowledgments

References

1. West JL. Nat. Mater. 2011; 10:727–729. [PubMed: 21941268]

2. Lutolf M. Adv. Mater. 2009; 21:3255–68. [PubMed: 20882496]

3. J. Cell Sci. 2010; 123:4201–13. [PubMed: 21123618]

4. Mann BK, Gobin AS, Tsai AT, Schmedlen RH, West JL. Biomaterials. 2001; 22:3045–3051. [PubMed: 11575479]

5. Khademhosseini A, Langer R. Proc. Natl. Acad. Sci. U. S. A. 2006; 103:2480–7. [PubMed: 16477028]

6. Moon J, Hahn M, Kim I. Tissue Eng., Part A. 2008; 15:579–85. [PubMed: 18803481]

7. Hardelauf H, Sisnaiske J, Taghipour-Anvari AA, Jacob P, Drabiniok E, Marggraf U, Frimat J-P, Hengstler JG, Neyer A, van Thriel C, West J. Lab Chip. 2011; 11:2763–71. [PubMed: 21709920]

8. Saik JE, Gould DJ, Keswani AH, Dickinson ME, West JL. Biomacromolecules. 2011; 12:2715–22. [PubMed: 21639150]

9. Walter J, Kern-Veits B, Huf J, Stolze B, Bonhoeffer F. Development. 1987; 101:685–96. [PubMed: 3503693]

10. Shi P, Nedelec S, Wichterle H, Kam LC. Lab Chip. 2010; 10:1005–10. [PubMed: 20358107]

11. von Philipsborn AC, Lang S, Loeschinger J, Bernard A, David C, Lehnert D, Bonhoeffer F, Bastmeyer M. Development. 2006; 133:2487. [PubMed: 16763203]

12. Shelly M, Cancedda L, Lim BK, Popescu AT, Cheng P-L, Gao H, Poo M-M. Neuron. 2011; 71:433–46. [PubMed: 21835341]

13. Mai J, Fok L, Gao H, Zhang X, Poo M-M. J. Neurosci. 2009; 29:7450. [PubMed: 19515913]

14. Withers GS, James CD, Kingman CE, Craighead HG, Banker GA. J. Neurobiol. 2006; 66:1183–94. [PubMed: 16858695]

15. Yates PA, Roskies AL, McLaughlin T, O'Leary DDM. J. Neurosci. 2001; 21:8548. [PubMed: 11606643]

16. Cornish T, Branch DW, Wheeler BC, Campanelli JT. Mol. Cell. Neurosci. 2002; 153:140–153. [PubMed: 12056845]

17. Feinerman O, Rotem A, Moses E. Nat. Phys. 2008; 4:967–973.

18. Feinerman O, Moses E. J. Neurosci. 2006; 26:4526–34. [PubMed: 16641232]

19. Killeen MT, Sybingco SS. Dev. Biol. 2008; 323:143–151. [PubMed: 18801355]

20. Bhagawati M, Lata S, Tampé R, Piehler J. J. Am. Chem. Soc. 2010; 132:5932–3. [PubMed: 20387883]

21. Hahn M, Miller J. Adv. Mater. 2005:2939–2942.

22. Shi P, Shen K, Kam LC. Dev. Neurobiol. 2007; 67:1765–76. [PubMed: 17659593]

23. Quist AP, Pavlovic E, Oscarsson S. Anal. Bioanal. Chem. 2005; 381:591–600. [PubMed: 15696278]

24. Azioune A, Storch M, Bornens M, Théry M, Piel M. Lab Chip. 2009; 9:1640–1642. [PubMed: 19458875]

25. Slater JH, Miller JS, Yu SS, West JL. Adv. Funct. Mater. 2011; 21:2798–2798.

26. Heinz WF, Hoh M, Hoh JH. Lab Chip. 2011; 11:3336–3346. [PubMed: 21858278]

27. Wissner-Gross ZD, Scott MA, Ku D, Ramaswamy P, Fatih Yanik M. Integr. Biol. 2011; 3:65–74.

28. Bélisle JM, Correia JP, Wiseman PW, Kennedy TE, Costantino S. Lab Chip. 2008; 8:2164–7. [PubMed: 19023482]

29. Bélisle JM, Kunik D, Costantino S. Lab Chip. 2009; 9:3580–3585. [PubMed: 20024039]

30. Patterson GH, Piston DW. Biophys. J. 2000; 78:2159–62. [PubMed: 10733993]

31. Dittrich PS, Schwille P. Appl. Phys. B: Lasers Opt. 2001; 73:829–837.

32. Chirico G, Cannone F, Baldini G, Diaspro A. Biophys. J. 2003; 84:588–98. [PubMed: 12524312]

33. Song L, Varma CA, Verhoeven JW, Tanke HJ. Biophys. J. 1996; 70:2959–68. [PubMed: 8744334]

34. Prime KL, Whitesides GM. J. Am. Chem. Soc. 1993; 115:10714–10721.

35. Rajnicek A, Britland S, McCaig C. J. Cell Sci. 1997; 110(Pt 2):2905–13. [PubMed: 9359873]

36. Dotti CG, Sullivan CA, Banker GA. J. Neurosci. 1988; 8:1454. [PubMed: 3282038]

37. Arimura N, Kaibuchi K. Nat. Rev., Neurosci. 2007; 8:194–205. [PubMed: 17311006]

38. Stenger DA, Hickman JJ, Bateman KE, Ravenscroft MS, Ma W, Pancrazio JJ, Shaffer K, Schaffner AE, Cribbs DH, Cotman CW. J. Neurosci. Methods. 1998; 82:167–173. [PubMed: 9700689]

39. Greene AC, Washburn CM, Bachand GD, James CD. Biomaterials. 2011; 32:8869–8860.

40. Peyrin J-M, Deleglise B, Saias L, Vignes M, Gougis P, Magnifico S, Betuing S, Pietri M, Caboche J, Vanhoutte P, Viovy J-L, Brugg B. Lab Chip. 2011; 11:3663–73. [PubMed: 21922081]

41. Xu C, Webb WW. J. Opt. Soc. Am. B. 1996; 13:481.

42. Donnert G, Eggeling C, Hell SW. Nat. Methods. 2007; 4:81–6. [PubMed: 17179937]

43. Polyzos I, Tsigaridas G, Fakis M, Giannetas V, Persephonis P. Opt. Lett. 2005; 30:2654. [PubMed: 16208931]

44. Cooper JM, Shen J, Young FM, Connolly P, Barker JR, Moores G. J. Mater. Sci.: Mater. Electron. 1994; 5:106–110.

45. Holden M, Cremer P. J. Am. Chem. Soc. 2003; 125:8074–8075. [PubMed: 12837056]

46. Decker C, Jenkins AD. Macromolecules. 1985; 18:1241–1244.

47. Hsiao Y-S, Lin C-C, Hsieh H-J, Tsai S-M, Kuo C-W, Chu C-W, Chen P. Lab Chip. 2011; 11:3674–3680. [PubMed: 21922117]

48. Mahmud G, Campbell CJ, Bishop KJM, Komarova YA, Chaga O, Soh S, Huda S, Kandere-Grzybowska K, Grzybowski BA. Nat. Phys. 2009; 5:606–612.

49. Ananthakrishnan R EA. Int. J. Biol. Sci. 2007; 3:303–317. [PubMed: 17589565]

50. Pasternack RM, Rivillon Amy S, Chabal YJ. Langmuir. 2008; 24:12963–71. [PubMed: 18942864]

51. Vogt AK, Stefani FD, Best A, Nelles G, Yasuda A, Knoll W, Offenhäusser A. J. Neurosci. Methods. 2004; 134:191–8. [PubMed: 15003385]

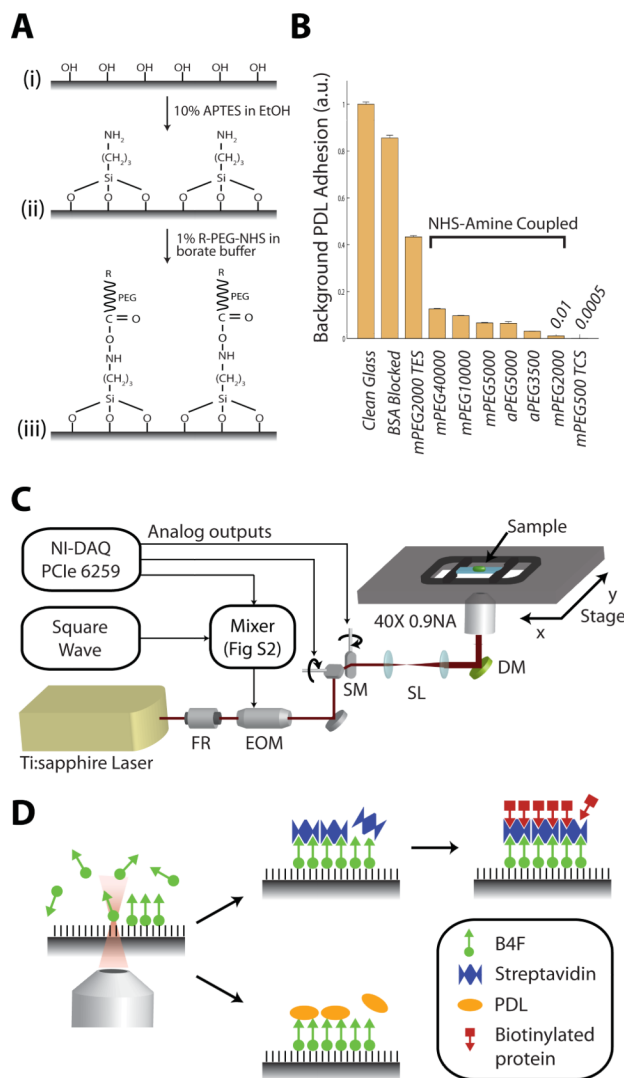52. Pirlo RK, Sweeney AJ, Ringeisen BR, Kindy M, Gao BZ. Biomicrofluidics. 2011; 5:13408. [PubMed: 21522498]

Figure 1. A high-speed laser micropatterning chemistry and system
(a) Glass is passivated with a PEG monolayer by first using APTES to form an amine-rich surface. R-PEG-NHS is then coupled to the amine surface to create a PEG monolayer, with a functionalized cap: R = CH$_3$ ('mPEG') or R = acrylate ('aPEG'). (b) Background PDL adhesion on different PEG monolayers, formed using various reaction chemistries, PEG chain-lengths and functionalized caps. (c) A femtosecond laser is scanned across the surface of a sample solution by means of x-y scanning mirrors. Laser power is modulated using an EOM. An encoded stepper-motor stage is used to pattern multiple fields of view. (d) Illumination of B4F causes it to crosslink to the underlying monolayer. The patterned biotin can then pull down streptavidin, or non-specifically pull down PDL from solution. TCS = trichlorosilane, TES = triethoxysilane, FR = Faraday rotor, EOM = Electro-optic modulator, SM = x-y Galvanometer scanning mirrors, SL = Scan lenses and beam expander, DM = Dichroic mirror, B4F = Biotin-4-fluorescein, PDL = Poly-D-lysine.
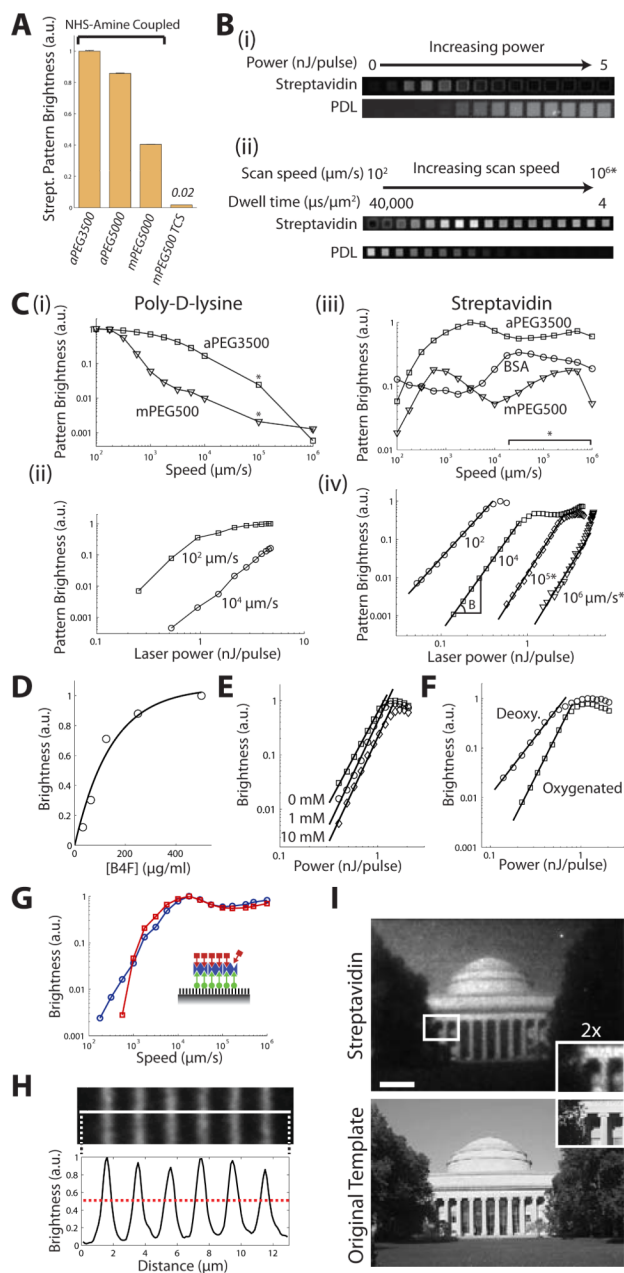
Figure 2. Multi-photon crosslinking of B4F to an aPEG3500 monolayer enables high-speed laser micropatterning of full-length proteins

Unless otherwise stated, all patterns are formed at scan speeds of 10 mm/s, laser powers of 5 nJ/pulse, and scan line separation of 0.25 µm. (a) Streptavidin pattern brightness on different PEG monolayers. (b) (i) 10 µm square patterns of PDL and streptavidin on an aPEG3500 monolayer at increasing laser powers, (ii) at increasing dwell-times. (c) (i) PDL pattern brightness on aPEG3500 and mPEG500 monolayers at varying scan speeds, (ii) PDL pattern brightness on aPEG3500 at varying laser powers, (iii) Streptavidin pattern brightness on aPEG3500 and mPEG500 monolayers, and BSA, at varying scan speeds, (iv) Streptavidin pattern brightness on aPEG3500 at varying laser powers, with fitted lines from the power law presented in Eq 2. (d) Varying streptavidin pattern brightness with B4F concentration, fitted with an exponential curve. (e) Streptavidin pattern brightness with varying bath

concentrations of L-ascorbic acid, fitted with lines from Eq 2. (f) Streptavidin pattern brightness using deoxygenated, or oxygenated B4F solutions, fitted with lines from Eq 2. (g) A comparison of streptavidin pattern brightness (blue circles) with biotinylated laminin pattern brightness (red squares). (h) Brightness profile, captured using a 1.4 NA oil immersion lens, of patterned streptavidin lines, separated by 2 μm. A full-width half maximum (FWHM) resolution of ~600 nm is demonstrated. (i) A streptavidin picture of the MIT dome and, for comparison, the original template used for the pattern. Insets are 2x magnified regions from the streptavidin pattern and original template. Scale bar = 10 μm. *=simulated speed using pulse-width modulation.
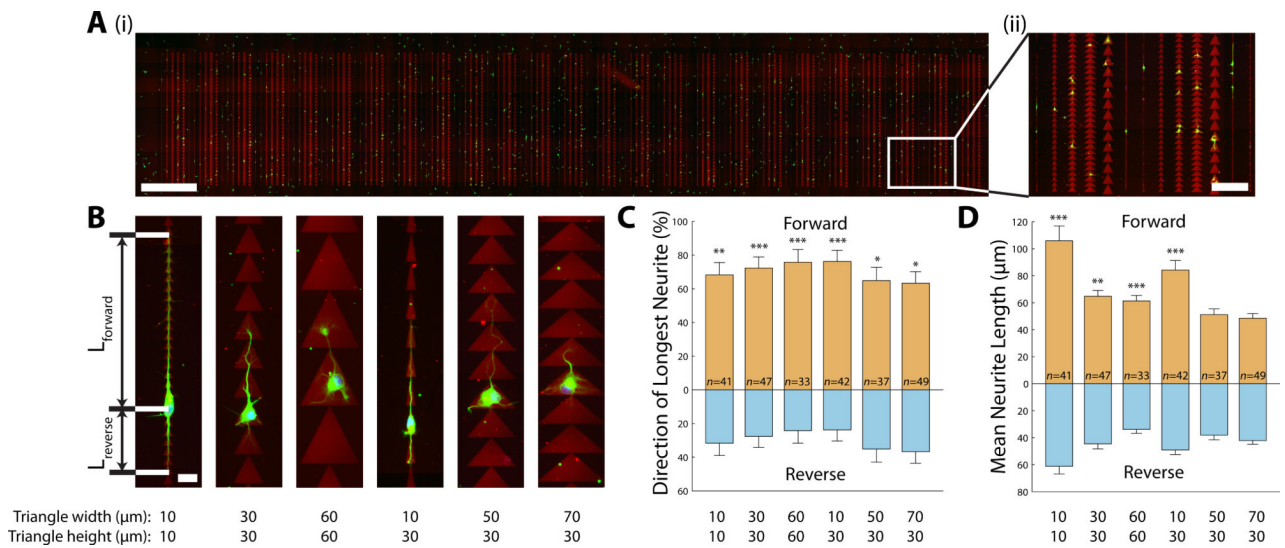
Figure 3. Strips of triangles of varying geometries can direct the polarization of single neurons
(a) A total of 15,000 patterned PDL triangles were formed over an area of 15×2.4 mm^2 (i) Scale bar = 1mm, (ii) Scale bar = 200 µm. (b) Neurons grown on triangles with varying heights and widths. The forward direction is defined as the direction from base to apex of the triangles. Scale bar = 20 µm (c) Proportion of neurons with their longest neurite in the 'forward' or 'reverse' direction. (d) Mean lengths of neurites in the 'forward' or 'reverse' direction. If multiple neurites were growing in one direction, the longest neurite length was used. For all graphs: * p < 0.05, ** p < 0.01, *** p < 0.001, comparing 'forward' with 'reverse' lengths.
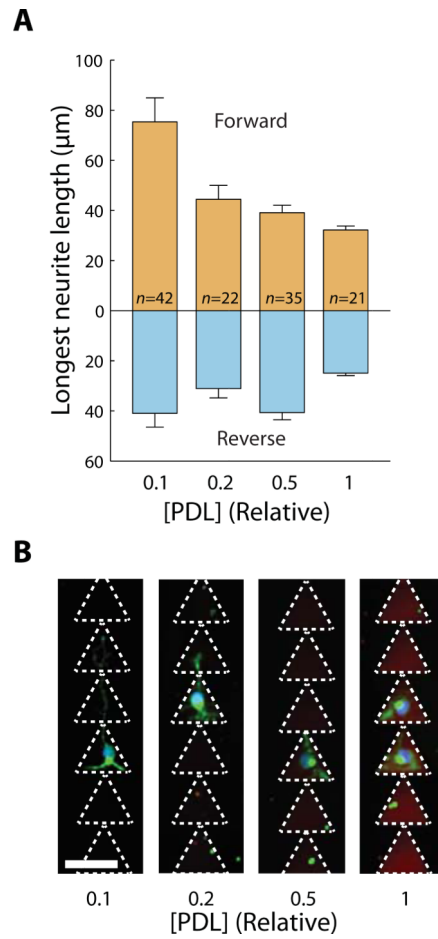
Figure 4. Lowering PDL density enables longer neurite outgrowth
(a) Mean length of neurites with varying PDL density on 50 µm triangles. (b) Images of neurons grown on varying densities of PDL. Scale bar = 50 µm.
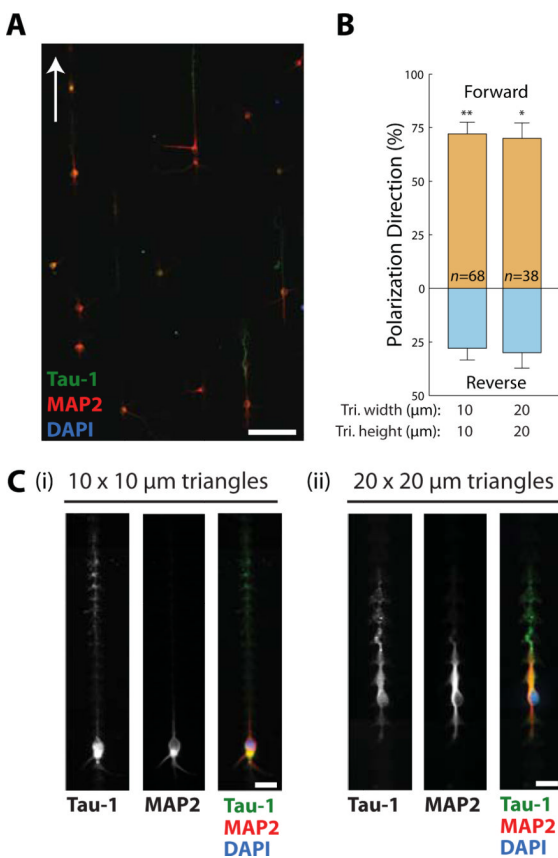
Figure 5. MAP2 and dephospho-Tau-1 immunostains confirm directed polarization of single neurons

(a) Tau-1 labeled axons (green) preferentially grow in the direction of the triangles (indicated by white arrow). Scale bar = 100 µm. (b) Distribution of axons growing in the forward or reverse directions for 10×10 µm and 20×20 µm triangles. (c) Tau-1 and MAP2 stained neurons extending on (i) 10×10 µm triangles, and (ii) 20×20 µm triangles. Scale bars = 20 µm. * $p < 0.01$, ** $p < 10^{-4}$.
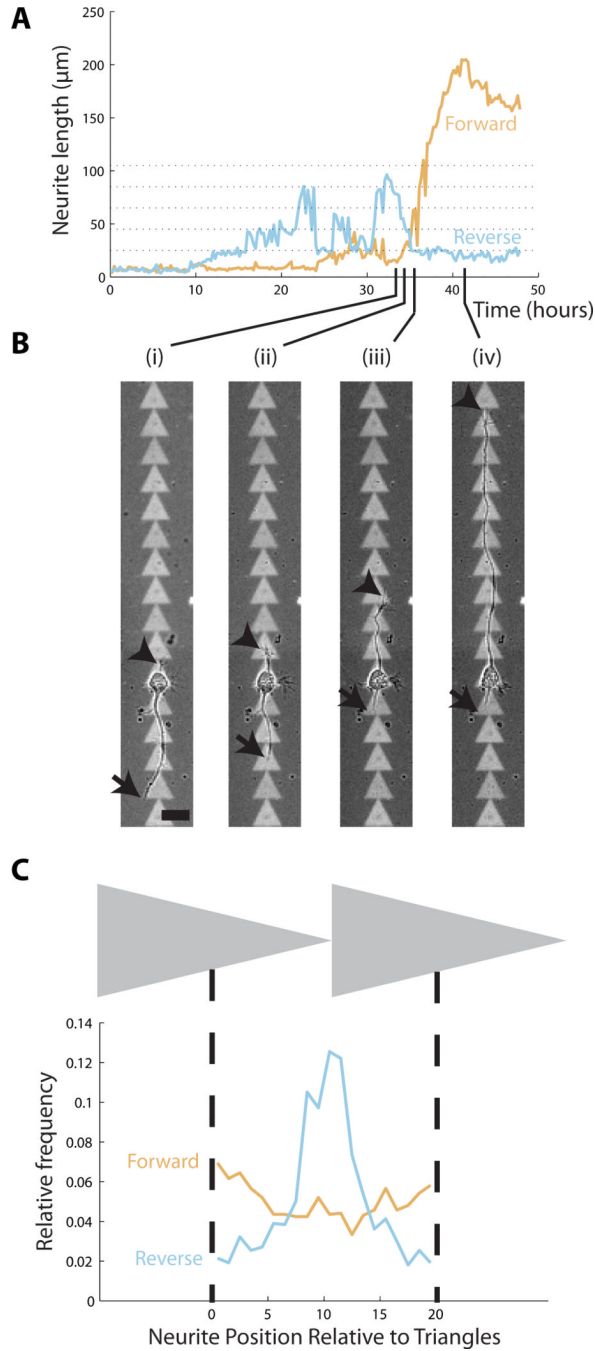
Figure 6. Time lapse imaging of neurite outgrowth on triangles reveals neurite polarization dynamics

(a) The length of forward and reverse projecting neurites from a neuron growing on 20 μm × 20 μm triangles (W × H) plotted over 48h. Images were taken at 14 min intervals. The dotted lines represent the lengths at which the reverse projecting neurite would cross between two triangles. (b) Images of the same neuron at four time points. (i) The reverse projecting neurite (arrow) runs into a 'dead-end'. (ii) The reverse projecting neurite retracts, while the forward projecting neurite (arrowhead) elongates. (iii-iv) The forward projecting neurite rapidly elongates while the reverse projecting neurite remains trapped. Scale bar = 20 μm. (c) A histogram derived from n=12 neurons, (10 forward polarized, 2 reverse

polarized), ~150 time points per neuron, showing frequency of neurite tip position as a function of its position relative to patterned triangles.
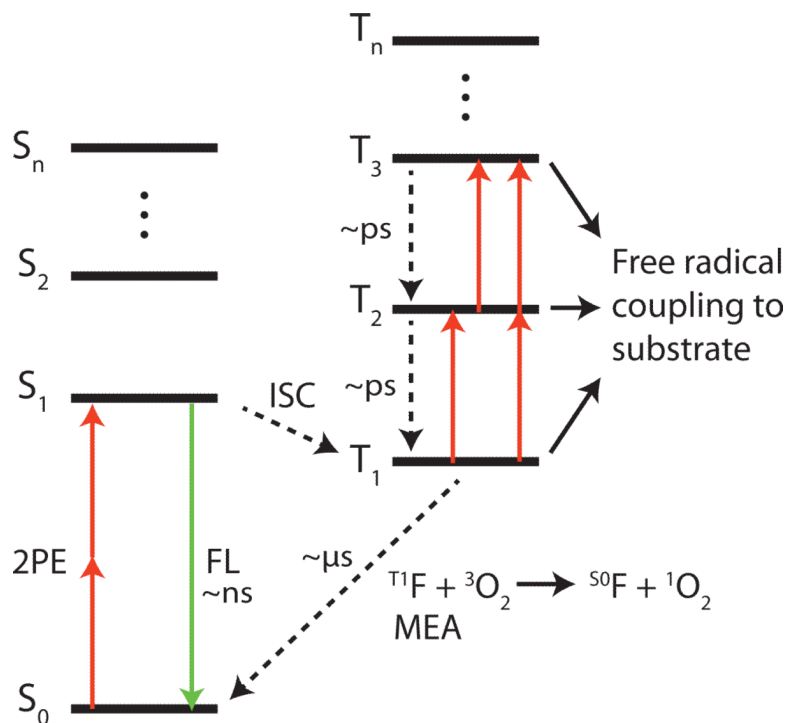
Figure 7. Jablonski diagram of a typical fluorophore
The fluorophore is first excited to the singlet-excited state (S_1) by two-photon excitation, then either relaxes back to ground state (S_0, ~ns timescale), or undergoes intersystem crossing into a more stable triplet-excited state (T_1). From this state, additional step-wise photon absorption leads to less stable higher energy triplet states ($T_{n > 1}$), and cross-linking to the underlying substrate. The triplet-excited state (T_1) relaxes back to ground state (S_0) via phosphorescence or internal conversion, or by reaction with dissolved triplet oxygen ($^3O_2$) or MEA. 2PE = two-photon excitation, FL = fluorescence emission, ISC = intersystem crossing, S_n = singlet-excited states of fluorophore, T_n = triplet-excited states of fluorophore.

Table 1

Photopatterning (pre-saturation) becomes faster and is driven by higher order multi-photon absorption events with increasing laser intensity

B in $S = a\tau P^B$ (obtained from the slopes of Fig 2c(iv) and Fig 2e,f) represents the average order of multi-photon processes that trigger the cross-linking of a B4F molecule to the substrate. At each scan speed, a range of laser powers was used at which measurable patterns were observed, without saturation of pattern brightness.

Scan speed μm/s	Pre-Saturation Laser Power Range (nJ/pulse)	[L-Ascorbic Acid] mM	Oxygenation	Multi-photon order (B) (dimensionless)
100	0.05 - 0.3	0	Ambient	2.5
10,000	0.2 - 0.8	0	Ambient	3.2
100,000 [*]	0.6 - 2	0	Ambient	3.6
1,000,000 [*]	1 - 4	0	Ambient	3.7
10,000	0.4 - 1	0	Ambient	3.4
10,000	0.4 - 1	1	Ambient	3.8
10,000	0.4 - 1	10	Ambient	3.9
10,000	0.2 - 0.8	0	Oxygenated	3.6
10,000	0.1 - 0.4	0	Deoxygenated	2.4

[*] =simulated speed using pulse-width modulation.

Table 2

Laser micropatterning by photobleaching of fluorophores

The quoted scan speeds represent those that produce 50% of the maximal brightness of streptavidin or PDL.

	Mechanism	Surface	PDL Patternable?	Protein Coupling	Scan Speed
Bélisle et al. (2008)	Single-photon	BSA passivated	No	Biotin-Streptavidin	10 µm/s
Wissner-Gross et al. (2011)	Multi-photon	Methyl-PEG (500 MW)	Yes	PDL (non-specific)	300 µm/s
This Paper	Multi-photon	Acryl-PEG (3,500 MW)	Yes	PDL (non-specific)	3,000 µm/s
This Paper	Multi-photon	Acryl-PEG (3,500 MW)	Yes	Biotin-Streptavidin	> 1,000,000 * µm/s

*
=simulated scan speed using pulse-width modulation.

Table 3

Methods for inducing directed polarization of neurons, or selectively redirecting growing axons of neurons

Mechanisms that induce directed polarization, such as that presented in this paper, use geometries that influence the rate of elongation of immature neurites to coordinate which neurite becomes the axon. Mechanisms using axon-redirection selectively permit passage of axons in one particular direction after neurons are already polarized.

	Geometry	Mechanism	Single cell?	Polarization or axon-redirection efficiency	Immunostaining confirmed?	Comments
Stenger et al. [38] (1998)	Speed bumps	Directing Polarization	Yes	76%	Yes	41% somal adherence to adhesion site
Vogt et al. [51] (2004)	Speed bumps	Directing Polarization	Yes	38% (p > 0.05)	No [***]	Patch clamp recordings to identify synapse direction
Feinerman et al. [17] (2008)	Triangle ratchets (millimeter scale)	Redirecting Axon Growth	No	75% [*]	No [**]	Demonstrated asymmetric electrical transmission
Peyrin et al. [40] (2011)	Funnel-shaped channels	Redirecting Axon Growth	No	96%	N/A	Used for neuronal co-cultures
Greene et al. [39] (2011)	Speed bumps	Directing Polarization	Yes	62%	No	75% somal adherence to adhesion site
Pirlo et al. [52] (2011)	Microfluidic 'snag' channels	Directing Polarization	Yes	77%	Yes	Manual cell placement using laser
This Paper	Triangle ratchets (micron scale)	Directing Polarization	Yes	72%	Yes	Cited efficiency is for 10×10 μm triangle geometry

[*] Computer simulated redirection efficiency.

[**] Directionality of signal transmission confirmed with electrical recordings.

[***] Polarization confirmed by patch clamp recording.